Chapter 7

Reiner-Rivlin nanoliquid flow past a spinning disk with Joule heating and non-uniform heat source using Bulirsch-Stoer algorithm *

7.1 Introduction

The current study is conducted to investigate the hydromagnetic flow of Reiner-Rivlin nanoliquids due to a rotating disk with non-uniform heat source and Joule heating effects inorder to optimize the heat transfer rate through Response surface methodology. The volume fraction of the nanoparticles on the disk surface is passively controlled by a realistic boundary condition. Using numerical and statistical methods, this work addresses the following research questions:

- How do the flow profiles vary due to the non-Newtonian nature?
- What effect does Joule heating have on the thermal boundary layer?
- How do temperature and space-dependent heat source parameters affect the heat transport phenomenon?
- How can the heat transfer rate be regulated by varying the influential effects?
- What is the sensitivity of the heat transport against the key factors?

*Published in: Waves in Random and Complex Media (Taylor & Francis), 2022; (early access)

7.2 Mathematical formulation

An electrically conducting non-transient Reiner-Rivlin nanofluid flow past a rotating disk is considered (see Fig. 7.1). The nanoliquid is present in the region above $z > 0$ and is incompressible. The axisymmetric spinning of the disk about the vertical axis ignores the derivatives along with tangential directions. The uniform spinning of the disk (with an angular velocity Ω) in the plane $z = 0$ imparts a swirling flow in the adjacent fluid layers. Here, $(u,\ v,\ w)$ are respectively the components of velocity vector projections along the radial (r), azimuthal (φ), and axial (z) directions. Let the temperature at the surface of the disk be T_w. Furthermore, T_∞ and C_∞ represent the ambient temperature and volume fraction of nanoparticles far from the disk. The centrifugal fan-like behaviour of the disk preserves the mass conservation principle by drawing the nanoliquid in the axial direction. The heterogeneous two-phase model is utilized to model the nanoliquid. Also, the fluid properties are considered to be constant in the system. The fluid is exposed to a uniform magnetic field of intensity B_0 along the axial direction and Joule heating effects are accounted. The governing equations to model the above problem are given below (see (Tabassum & Mustafa, 2018), (Imtiaz, Kiran, Hayat, & Alsaedi, 2019), (Lin, Ghaffari, et al., 2021)):

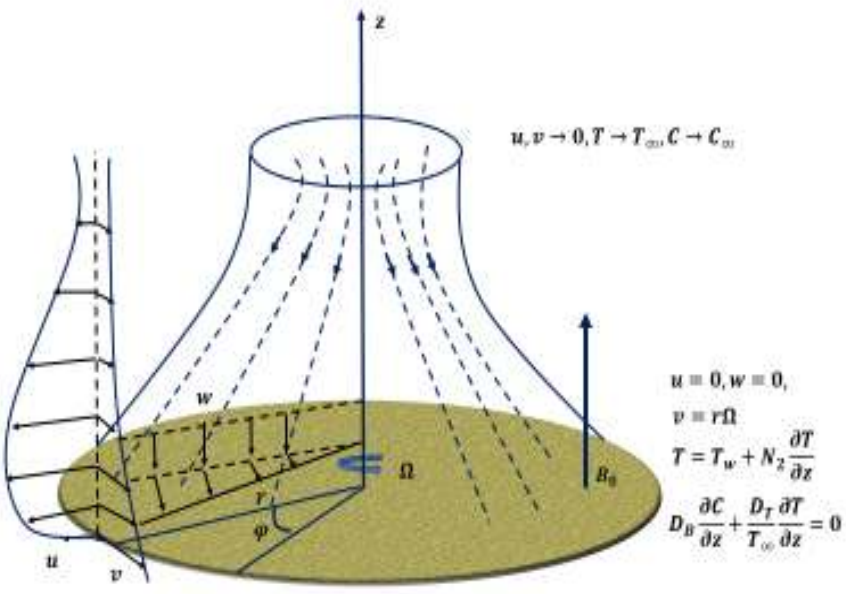

Figure 7.1: *Physical configuration*

$$\frac{\partial u}{\partial r} + \frac{u}{r} + \frac{\partial w}{\partial z} = 0, \tag{7.2.1}$$

$$\rho_f\left(u\frac{\partial u}{\partial r}+w\frac{\partial u}{\partial z}-\frac{v^2}{r}\right)=\frac{\partial \tau_{rr}}{\partial r}+\frac{\partial \tau_{zr}}{\partial z}+\frac{(\tau_{rr}-\tau_{\varphi\varphi})}{r}-\sigma_f B_0^2 u, \tag{7.2.2}$$

$$\rho_f\left(u\frac{\partial v}{\partial r}+w\frac{\partial v}{\partial z}+\frac{uv}{r}\right)=\frac{1}{r^2}\frac{\partial}{\partial r}\left(r^2\tau_{r\varphi}\right)+\frac{\partial \tau_{z\varphi}}{\partial z}+\frac{(\tau_{r\varphi}-\tau_{\varphi r})}{r}-\sigma_f B_0^2 v, \tag{7.2.3}$$

$$\rho_f\left(u\frac{\partial w}{\partial r}+w\frac{\partial w}{\partial z}\right)=\frac{1}{r}\frac{\partial}{\partial r}\left(r\tau_{rz}\right)+\frac{\partial \tau_{zz}}{\partial z}, \tag{7.2.4}$$

$$\begin{aligned} u\tfrac{\partial T}{\partial r}+w\tfrac{\partial T}{\partial z}=\alpha_m\left(\tfrac{\partial^2 T}{\partial r^2}+\tfrac{1}{r}\tfrac{\partial T}{\partial r}+\tfrac{\partial^2 T}{\partial z^2}\right)+\tfrac{(\rho c)_p}{(\rho c)_f}\left\{D_B\left(\tfrac{\partial T}{\partial r}\tfrac{\partial C}{\partial r}+\tfrac{\partial T}{\partial z}\tfrac{\partial C}{\partial z}\right)\right. \\ \left.+\tfrac{D_T}{T_\infty}\left(\left(\tfrac{\partial T}{\partial r}\right)^2+\left(\tfrac{\partial T}{\partial z}\right)^2\right)\right\}+\tfrac{1}{(\rho c)_f}q'''+\tfrac{\sigma_f B_0^2}{(\rho c)_f}\left(u^2+v^2\right), \end{aligned} \tag{7.2.5}$$

$$u\frac{\partial C}{\partial r}+w\frac{\partial C}{\partial z}=D_B\left(\frac{\partial^2 C}{\partial r^2}+\frac{1}{r}\frac{\partial C}{\partial r}+\frac{\partial^2 C}{\partial z^2}\right)+\frac{D_T}{T_\infty}\left(\frac{\partial^2 T}{\partial r^2}+\frac{1}{r}\frac{\partial T}{\partial r}+\frac{\partial^2 T}{\partial z^2}\right), \tag{7.2.6}$$

q''' is the non-uniform heat generation /absorption term that is modeled as $q'''=\frac{k_f\Omega}{\nu_f}\left[\frac{A(T_w-T_\infty)}{\Omega r}u+B\ (T-T_\infty)\right]$, where A and B denote respectively the space-dependent and temperature-dependent heat source/sink parameters. The internal heat generation mechanism without an external heat source has a major role in medical and industrial applications. Current flow in a conducting fluid augments the temperature of the fluid and therefore, the Joule heating effect is incorporated via the last term in Eqn. 7.2.5. The nanoparticle volume fraction at the surface of the disk is passively controlled. The disk is rigid which does not allow fluid penetration and viscous dissipative forces are ignored due to negligible effects. The thermal disparity between the disk and the nanoliquid associated with the surface is incorporated through the thermal jump condition.

Boundary conditions:

$$\left.\begin{aligned} &\text{At } z=0:\ u=0, && v=v_w=r\Omega, && w=0,\\ &T=T_w+N_2\tfrac{\partial T}{\partial z}\ , && D_B\tfrac{\partial C}{\partial z}+\tfrac{D_T}{T_\infty}\tfrac{\partial T}{\partial z}=0\ . \end{aligned}\right\} \tag{7.2.7}$$

$$As\ \ z\to\infty: u\to 0, \qquad v\to 0, \qquad T\to T_\infty, \qquad C\to C_\infty, \qquad p\to p_\infty. \tag{7.2.8}$$

Due to the stress tensor symmetry, the second last term in Eqn. 7.2.3 is ignored. The following constitutive relation is used to model the rheological properties of the Reiner-Rivlin nanoliquid:

$$\tau_{ij}=-p\delta_{ij}+\mu_f e_{ij}+\mu_c e_{ik}e_{kj}(e_{jj}=0).(see(Tabassum\ \&Mustafa,2018)): \tag{7.2.9}$$

The influence of stress across velocity gradients leads to cross-viscosity, a property of the Reiner-Rivlin nanofluid considered in the study. Here, the rate of strain (deformation) tensor is denoted by $e_{ij} = \frac{\partial u_i}{\partial x_j} + \frac{\partial u_j}{\partial x_i}$, Kronecker delta symbol is denoted by δ_{ij}, $\text{cross} - \text{viscosity}$ coefficient is denoted by μ_c, coefficient of viscosity is denoted by μ_f and pressure is denoted by p. The stress tensors (τ_{ij}) of this liquid are given as follows (see (Tabassum & Mustafa, 2018)):

$$\tau_{rr} = -p + \mu_f \left(2\frac{\partial u}{\partial r}\right) + \mu_c \left\{4\left(\frac{\partial u}{\partial r}\right)^2 + \left(\frac{\partial v}{\partial r} - \frac{v}{r}\right)^2 + \left(\frac{\partial u}{\partial z} + \frac{\partial w}{\partial r}\right)^2\right\}, \quad (7.2.10)$$

$$\begin{aligned}\tau_{zr} = \mu_f \left(\tfrac{\partial u}{\partial z} + \tfrac{\partial w}{\partial r}\right) + \mu_c \left\{\left(2\tfrac{\partial u}{\partial r}\right)\left(\tfrac{\partial u}{\partial z} + \tfrac{\partial w}{\partial r}\right) + \left(\tfrac{\partial v}{\partial r} - \tfrac{v}{r}\right)\left(\tfrac{\partial v}{\partial z}\right)\right\} + \\ \mu_c \left\{\left(\tfrac{\partial u}{\partial z} + \tfrac{\partial w}{\partial r}\right)\left(2\tfrac{\partial w}{\partial z}\right)\right\},\end{aligned} \quad (7.2.11)$$

$$\tau_{\varphi\varphi} = -p + \mu_f \left(\frac{2u}{r}\right) + \mu_c \left\{\frac{4u^2}{r^2} + \left(\frac{\partial v}{\partial r} - \frac{v}{r}\right)^2 + \left(\frac{\partial v}{\partial z}\right)^2\right\}, \quad (7.2.12)$$

$$\begin{aligned}\tau_{r\varphi} = \mu_f \left(\tfrac{\partial v}{\partial r} - \tfrac{v}{r}\right) + \mu_c \left\{\left(2\tfrac{\partial u}{\partial r}\right)\left(\tfrac{\partial v}{\partial r} - \tfrac{v}{r}\right) + \left(\tfrac{\partial v}{\partial r} - \tfrac{v}{r}\right)\left(\tfrac{2u}{r}\right)\right\} + \\ \mu_c \left\{\left(\tfrac{\partial u}{\partial z} + \tfrac{\partial w}{\partial r}\right)\left(\tfrac{\partial v}{\partial z}\right)\right\},\end{aligned} \quad (7.2.13)$$

$$\tau_{z\varphi} = \mu_f \frac{\partial v}{\partial z} + \mu_c \left\{\left(\frac{\partial v}{\partial r} - \frac{v}{r}\right)\left(\frac{\partial u}{\partial z} + \frac{\partial w}{\partial r}\right) + 2\left(\frac{u}{r}\right)\left(\frac{\partial v}{\partial z}\right) + 2\left(\frac{\partial v}{\partial z}\right)\left(\frac{\partial w}{\partial z}\right)\right\}, \quad (7.2.14)$$

$$\tau_{zz} = -p + \mu_f \left(2\frac{\partial w}{\partial z}\right) + \mu_c \left\{\left(\frac{\partial u}{\partial z} + \frac{\partial w}{\partial r}\right)^2 + \left(\frac{\partial v}{\partial z}\right)^2 + 4\left(\frac{\partial w}{\partial z}\right)^2\right\} \quad (7.2.15)$$

The axial, radial, and azimuthal velocity components rely upon radial and normal spatial coordinates (r and z). Pressure along z-direction is considered in the system. The well-known von-Karman similarity variables are adopted as follows (see (Tabassum & Mustafa, 2018)):

$$(u, v, w) = \left(r\Omega F'(\zeta), r\Omega G(\zeta), -2\sqrt{\nu_f \Omega}\, F(\zeta)\right), \ \zeta = \frac{z}{r} Re^{1/2}, \quad (7.2.16)$$

$$(p, T, C) = (p_\infty - \Omega \mu_f P(\zeta), T_\infty + (T_w - T_\infty)\theta(\zeta), C_\infty + C_\infty \phi(\zeta)) \quad (7.2.17)$$

Thereby, the following equations are obtained:

$$F''' - F'^2 + 2FF'' + G^2 - K\left[2F'F''' - F''^2 + G'^2\right] - MF' = 0, \quad (7.2.18)$$

$$G'' - 2F'G + 2G'F - 2K\left[F'G'' - F^{''}G'\right] - MG = 0, \tag{7.2.19}$$

$$P' - 2F'' - 4FF' + 28\ KF'F'' + 2Re\ K\left\{F''F''' + G'G''\right\} = 0 \tag{7.2.20}$$

$$\theta'' + Pr_f\left[2\theta'F + Nb\ \theta'\phi' + Nt\ \theta'^2 + Ec\ M\left(F'^2 + G^2\right)\right] + A\ F' + B\ \theta = 0, \tag{7.2.21}$$

$$\phi'' + \frac{Nt}{Nb}\theta'' + 2Sc\ F\phi' = 0. \tag{7.2.22}$$

With the following conditions:

$$\left.\begin{array}{c} \text{At } \zeta = 0: \ F = 0,\ F' = 0,\ G = 1, \\ \theta = 1 + \gamma\theta',\ \phi' + \frac{Nt}{Nb}\theta' = 0. \end{array}\right\} \tag{7.2.23}$$

$$As\ \ \zeta \to \infty : F' \to 0, G \to 0, \theta \to 0, \phi \to 0,\ P \to 0. \tag{7.2.24}$$

It can be noted that Eqn. 7.2.1 describes a self-satisfying continuity equation and Eqn. 7.2.20 can be used to analyze the pressure distribution, but this is beyond the scope of the current study. The following are the dimensionless parameters of the current study:
$Sc = \frac{\nu_f}{D_B}$ (Schmidt number), $Pr_f = \frac{\nu_f}{\alpha_m}$ (Prandtl number), $K = \frac{\mu_c\Omega}{\mu_f}$ (Reiner-Rivlin material parameter), $\gamma = \left(\frac{\Omega}{\nu_f}\right)^{\frac{1}{2}} N_2$ (Thermal slip parameter), $M = \frac{\sigma_f B_0^2}{\rho_f\Omega}$ (Hartmann number), $Ec = \frac{v_w^2}{c_f(T_w - T_\infty)}$ (Eckert number), $Nb = \frac{(\rho c)_p D_B C_\infty}{(\rho c)_f \nu_f}$ (Brownian motion parameter), $Nt = \frac{(\rho c)_p D_T (T_w - T_\infty)}{(\rho c)_f T_\infty \nu_f}$ (Thermophoresis parameter), and $Re = \frac{\Omega r^2}{\nu_f}$ (Local Reynolds number).
Nu_r indicates the reduced Nusselt number which measures the convective to conductive heat transfer ratio. Also, a resistive force (friction) by the relative movement of fluid layers at the rotating disk causes surface drag which is measured using skin friction coefficient (C_f). The Nusselt number (N_u) and skin friction given as follows ((Tabassum & Mustafa, 2018)):

$$\left.\begin{array}{c} Nu = \frac{rq_w}{k_f(T_w - T_\infty)}, \\ C_f = \frac{\sqrt{\tau_r^2 + \tau_\varphi^2}}{\rho_f v_w^2}. \end{array}\right\} \tag{7.2.25}$$

where heat flux is denoted by q_w, radial wall stress by τ_r, and azimuthal wall stress by τ_φ. Using the Eqns. (7.2.16-7.2.17), Eqn. (7.2.25) yields the reduced Nusselt number (Nu_r) and skin friction coefficient (Cf_r) as follows:

$$\left.\begin{aligned} Nu_r = Re^{-\frac{1}{2}} Nu = -\theta'(0), \\ Cf_r = Re^{\frac{1}{2}} C_f = \sqrt{(F''(0))^2 + (G'(0))^2}. \end{aligned}\right\} \tag{7.2.26}$$

7.3 Numerical solution

The equations (7.2.18)-(7.2.19) and (7.2.21)-(7.2.22) is a boundary value problem (BVP) which does not possess an analytical solution. So, the Bulirsch-Stoer algorithm and Newton-Raphson method are employed. By substituting $y_1 = F, y_2 = F', y_3 = F'', y_4 = G, y_5 = G', y_6 = \theta, y_7 = \theta', y_8 = \phi, y_9 = \phi'$, one can get the following equations:

$$\left.\begin{aligned} y_1' &= y_2, \\ y_2' &= y_3, \\ y_3' &= \tfrac{y_2^2 - 2y_1y_3 - y_4^2 - Ky_3^2 + Ky_5^2 + My_2}{1-2Ky_2}, \\ y_4' &= y_5, \\ y_5' &= \tfrac{2y_2y_4 - 2y_1y_5 - 2Ky_3y_5 + My_4}{1-2Ky_2}, \\ y_6' &= y_7, \\ y_7' &= \{-Pr_f\,[2y_1y_7 + Nb\ y_7y_9 + Nt\ y_7^2 + Ec\ M\ \ (y_2^2 + y_4^2)] \\ &\quad -Ay_2 - By_6\}, \\ y_8' &= y_9, \\ y_9' &= \left\{-\left(\tfrac{N_t}{N_b}\right) y_7' - 2Sc\ y_1\ y_9\right\}. \end{aligned}\right\} \tag{7.3.1}$$

The following initial conditions are considered:

$$\left.\begin{aligned} y_1(0) = 0, y_2(0) = 0,\ \ y_3(0) = h_1, y_4(0) = 1, y_5(0) = h_2, \\ y_6(0) = 1 + \gamma\ h_3,\ \ y_7(0) = h_3, y_8(0) = h_4,\ \ y_9(0) = -\tfrac{Nt}{Nb}\ h_3. \end{aligned}\right\} \tag{7.3.2}$$

where $h_1, h_2, h_3,$ and h_4 are calculated by utilizing the Newton-Raphson method by using suitable guess values. Numerical solutions are generated with an error tolerance of 10^{-6} and step size of 0.01. ζ_∞ has been restricted to 15 as the further increment of the domain has a negligible effect. The accuracy of the adopted numerical method has been validated by comparing the limiting case of the present problem (see Table 7.1) with the previously published results by Turkyilmazoglu and Senel (Turkyilmazoglu & Senel, 2013).

Table 7.1: *Comparison of* $F''(0), G'(0), F(\infty)$, *and*$-\theta'(0)$ *with* $K = 0,\ M = 0,\ Ec = 0,\ A = 0,\ B = 0,\ Nt = 0, Sc = 0, Nb \to 0\ , Pr_f = 0.72^a$, *and* $Pr_f = 6^b$.

	Runge-Kutta-4 method (Turkyilmazoglu & Senel, 2013)	Bulirsch-Stoer algorithm
$F''(0)$	0.51023262	0.51023239
$G'(0)$	-0.61592201	-0.61592187
$F(\infty)$	0.44223705	0.44221609
$-\theta'(0)^a$	0.3285701	0.32861104
$-\theta'(0)^b$	0.92118503	0.92123523

7.4 Results and Discussion

The impact of the Reiner-Rivlin material parameter (K), Hartmann number(M), Schmidt number (Sc), thermophoresis parameter (Nt), Space-dependent heat source parameter (A), Eckert number (Ec), thermal slip parameter (γ), and temperature-dependent heat source parameter (B) is studied on the radial velocity ($F'(\zeta)$), azimuthal velocity ($G(\zeta)$), temperature ($\theta(\zeta)$) and volume fraction of nanoparticles ($\phi(\zeta)$) profiles respectively. The Prandtl number is chosen as 7 throughout the analysis.

Fig. 7.2-7.5 depicts the impression of M on $F'(\zeta)$, $G(\zeta)$, $\theta(\zeta)$ and $\phi(\zeta)$ profiles. An increase in M generates a Lorentz force, a resistive force against the fluid flow that retards the nanoliquid flow in radial and azimuthal directions. The drag coefficient at the surface of the disk grows due to the opposing force that enhances the fluid temperature (see Fig. 7.4). Fig. 7.5 displays a mixed response in nanoparticle volume fraction with magnification in M.

Fig. 7.6-7.9 reveals the response in $F'(\zeta)$, $G(\zeta), \theta(\zeta)$, and $\phi(\zeta)$ profiles concerning K. Viscoelastic nature of the nanoliquid enhances with increment in K. Fig. 7.6 depicts a negative impact in radial velocity profile with growing values of K and the trend reverses far from the disk. The peak in the velocity curve is due to weak non-Newtonian characteristics. Axial flow reduces due to the viscoelastic nature of

the nanoliquid and a small amount of fluid is drawn in the radial direction even though centrifugal force works. Rotation inertial effects get stronger with mounting values of K that elevate the azimuthal velocity profile (See Fig. 7.7). Fig. 7.8 delineates an increase in temperature with augmenting values of K. Less amount of cold ambient fluid is drawn towards the disk which rises the nanoliquid temperature. The nanoparticle volume fraction of the nanoliquid shows a dual nature as shown in Fig. 7.9. Maximum nanoparticle volume fraction is noticed far from the disk.

Fig. 7.10 shows a positive impact of Ec on $\theta(\zeta)$. Joule heating has a predom-

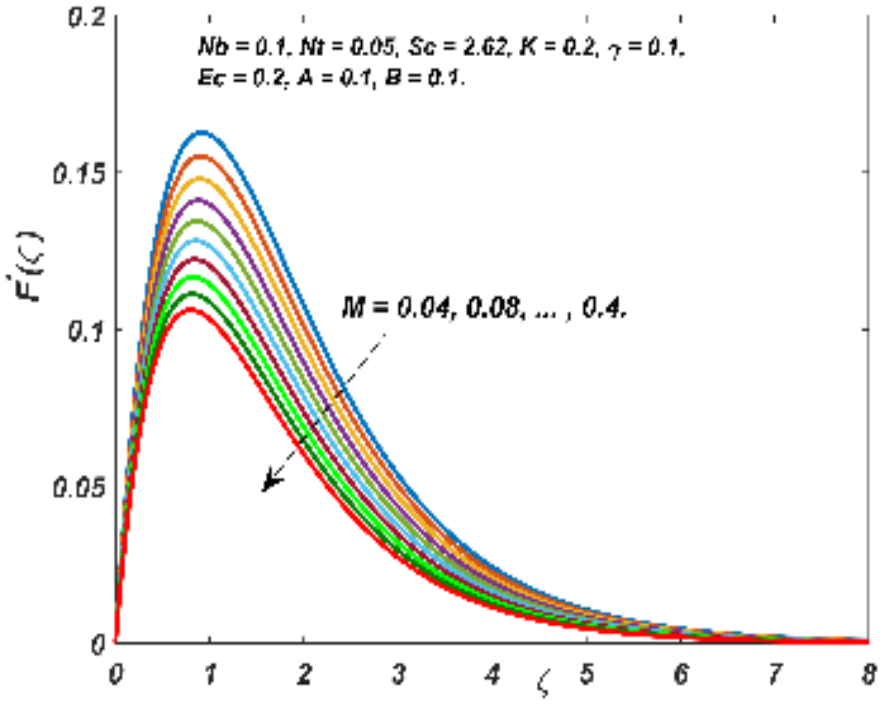

Figure 7.2: *Response in $F'(\zeta)$ for distinct M.*

inant impact on the thermal boundary layer thickness. Kinetic energy enhances with Ec that fuels the internal friction of nanoparticles followed by a rise in the temperature profile. Fig. 7.11 explains a mixed impact of Sc with $\phi(\eta)$. Nanoparticle volume fraction profile decreases with Sc far from the disk and it depicts an increasing functional relationship near the disk. Physically, it is due to depletion in molecular diffusion and migration of nanoparticles with magnification in Sc. Fig. 7.12 delineates a positive response of A & B on $\theta(\zeta)$. Temperature profile enhances with augmentation in A & B. An increase in the space and temperature-dependent heat source (A & B) produces additional heat energy to the nano liquid flow which

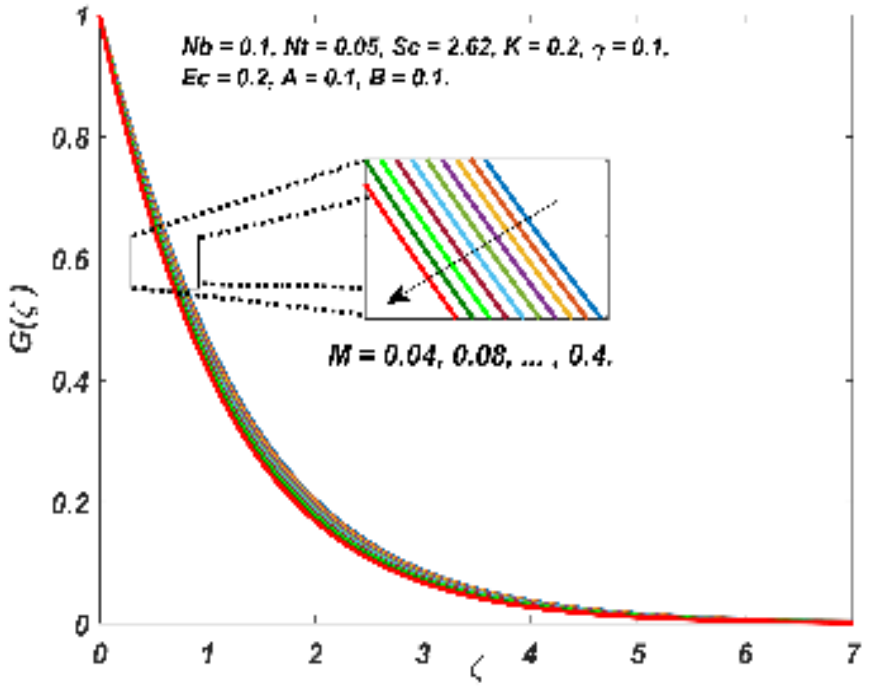

Figure 7.3: *Response in $G(\zeta)$ for distinct M.*

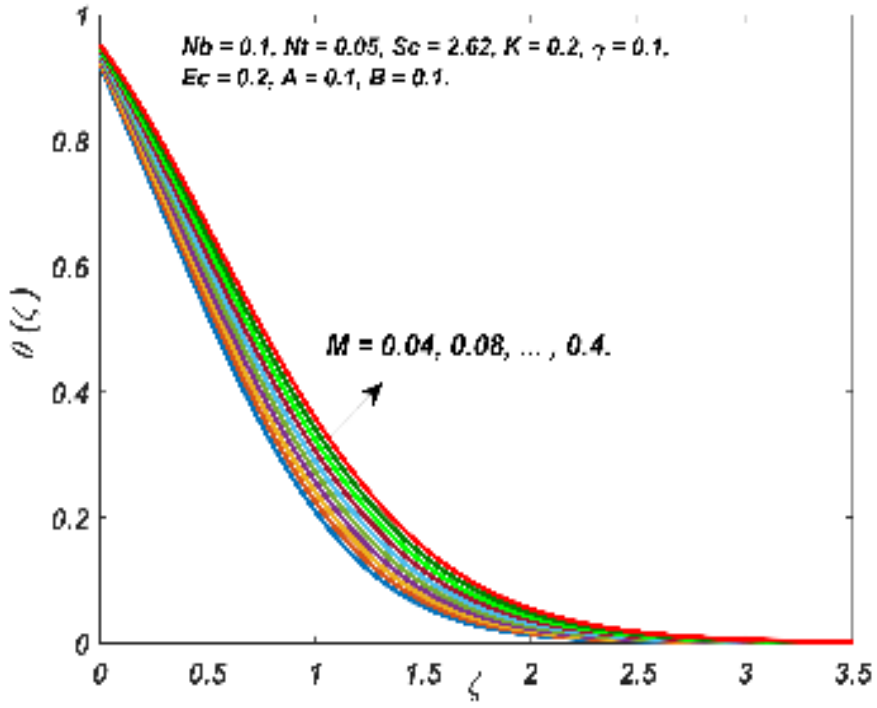

Figure 7.4: *Response in $\theta(\zeta)$ for distinct M.*

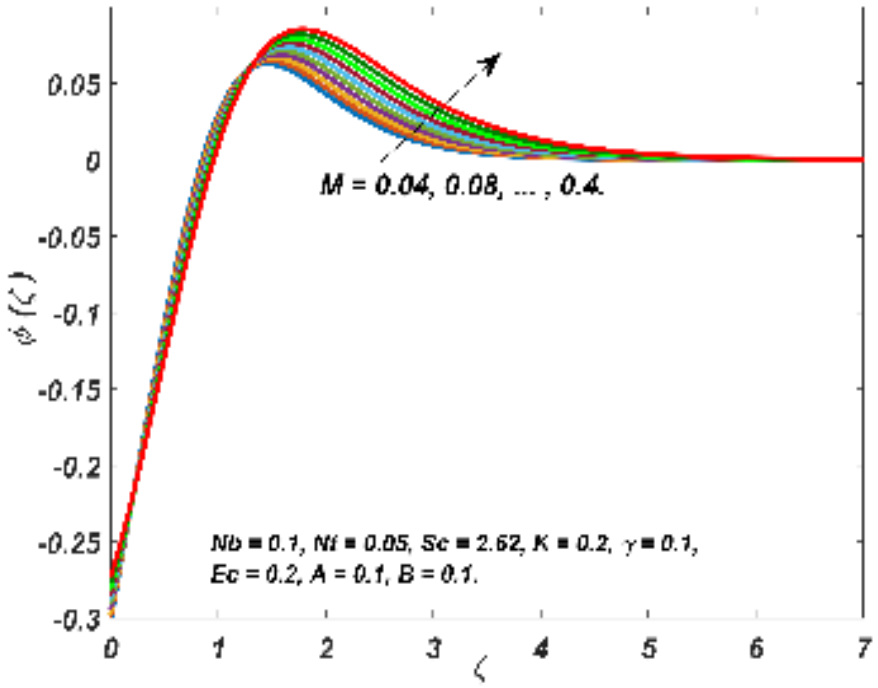

Figure 7.5: *Response in $\phi(\zeta)$ for distinct M.*

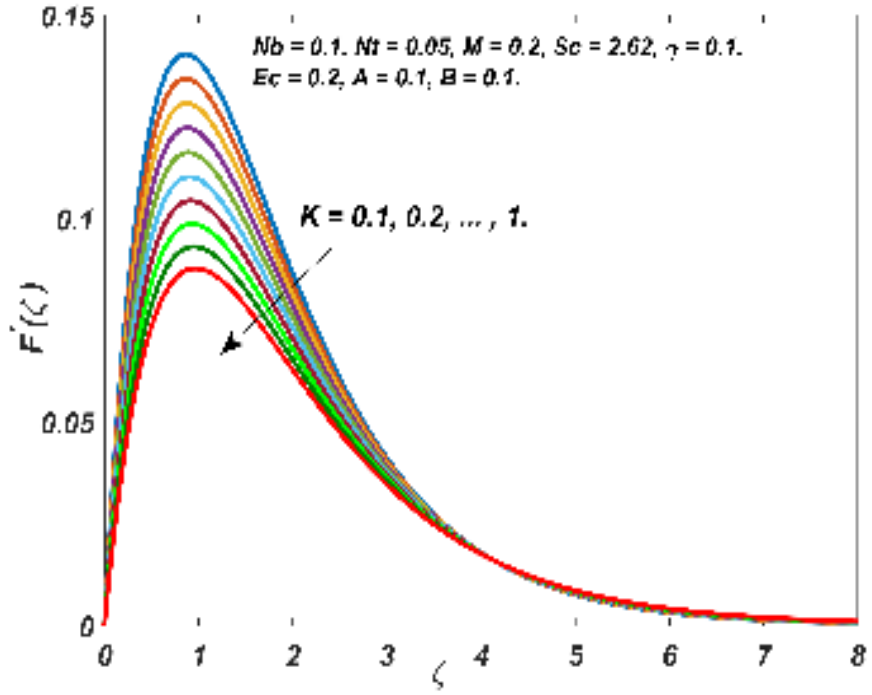

Figure 7.6: *Response in $F'(\zeta)$ for distinct K.*

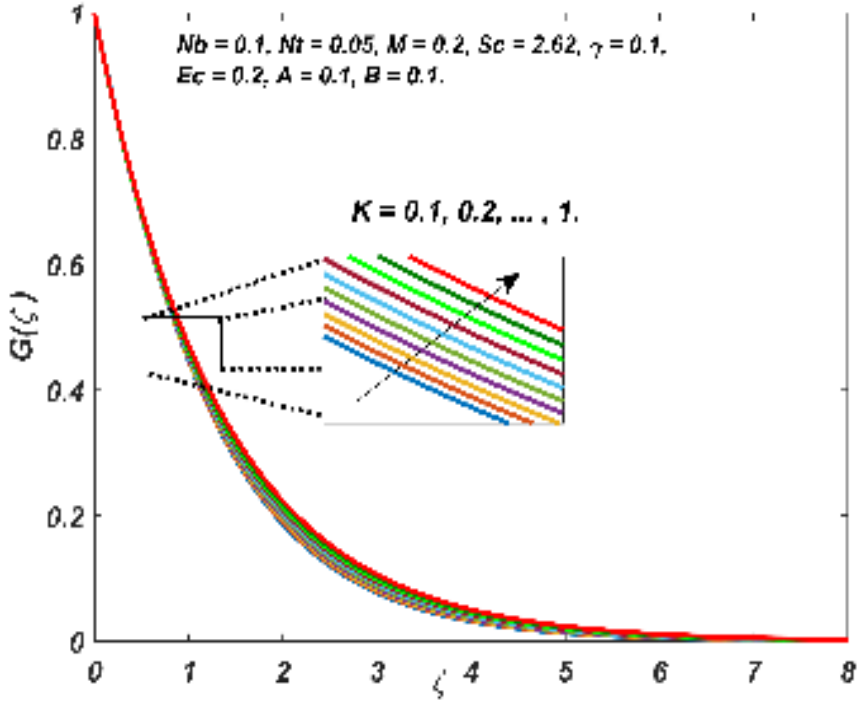

Figure 7.7: *Response in $G(\zeta)$ for distinct K.*

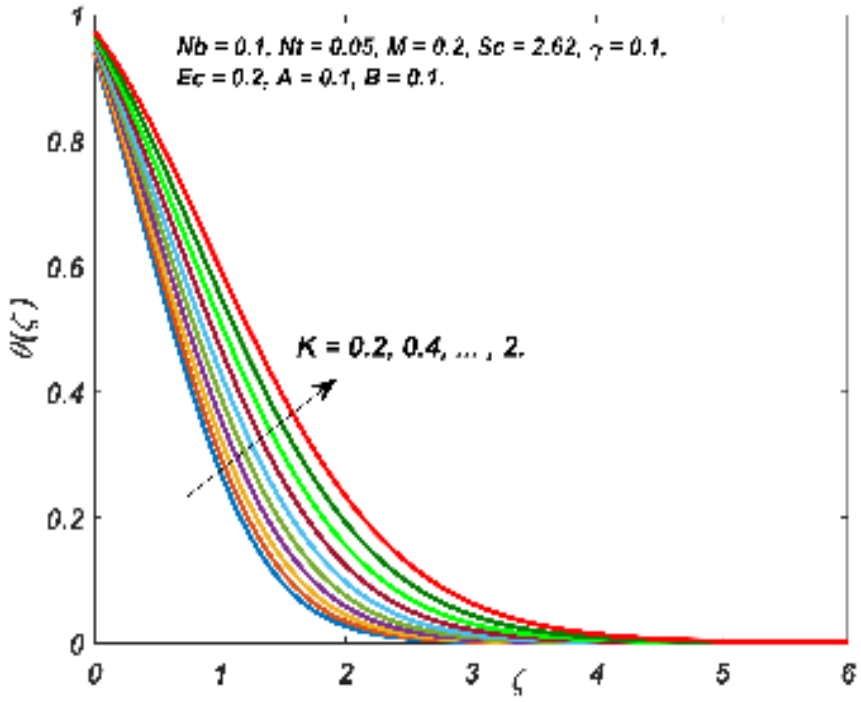

Figure 7.8: *Response in $\theta(\zeta)$ for distinct K.*

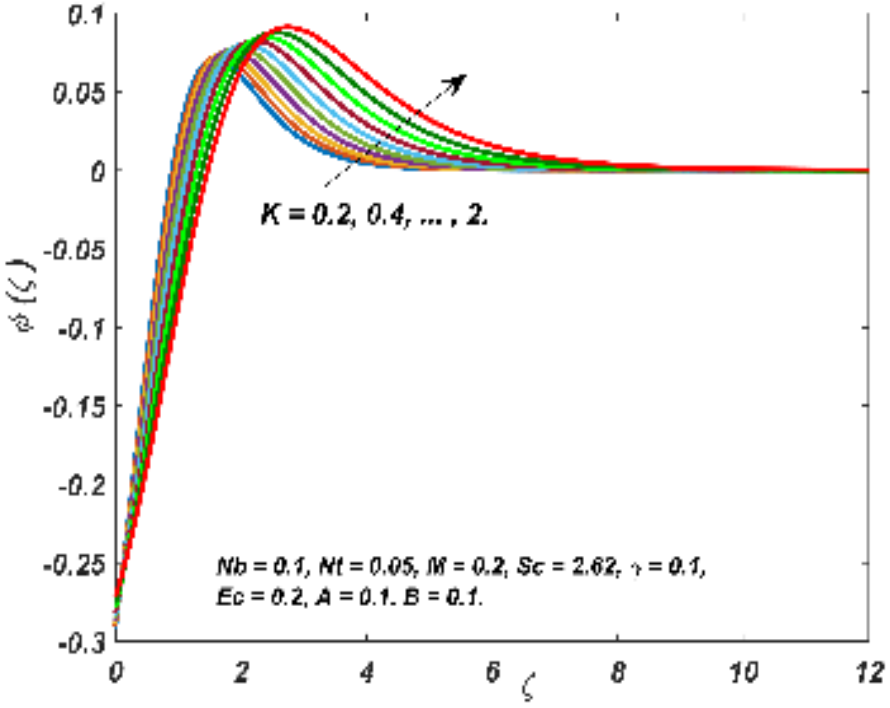

Figure 7.9: *Response in $\phi(\zeta)$ for distinct K.*

escalates the thermal boundary layer thickness.

Fig. 7.13-7.14 discloses the influence of Nt on $\theta(\zeta)$ and $\phi(\zeta)$ profiles. Augmentation in Nt elevates the temperature whereas the nanoparticle volume fraction profile shows a mixed character with Nt. A negative impact of nanoparticle volume fraction with Nt is observed near the disk and the nature reverses far from the disk. Physically, an increment in Nt produces thermophoresis force which moves the hot fluid particles to the colder ambient region. Fig. 7.15 juxtaposes the consequence of $\theta(\zeta)$ with variation in γ. An increase in thermal slip parameter extrapolates interfacial fluid temperature followed by a thermal resistance which depreciates further thermal transport in fluids and hence $\theta(\zeta)$ lowers.

Three-dimensional plots are used to examine the simultaneous impact of two parameters on the frictional drag and heat transfer rate as depicted in Figs. 7.16-7.19. A maximum frictional drag was observed for low K and high M values. Physically, it is due to high Lorentz force and minimum cross-viscosity. The highest heat transfer rate occurs at low A and B parameter values (see Fig. 7.17). Augmentation in A & B supplements additional heat energy to the nanoliquid that in turn minimizes the thermal difference. Fig. 7.18 delineates the discrepancy of Nusselt number with

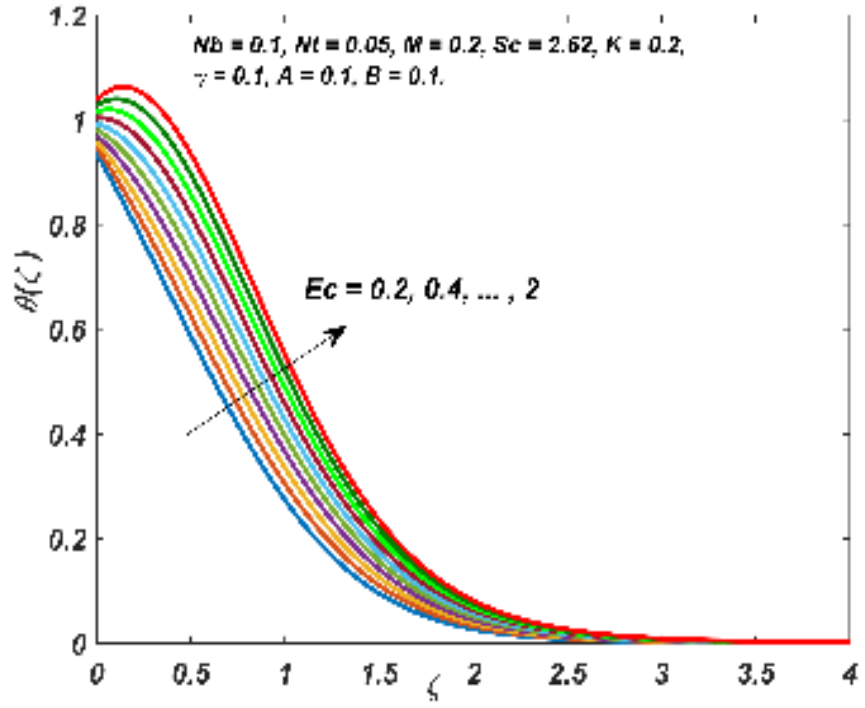

Figure 7.10: *Response in $\theta(\zeta)$ for distinct Ec.*

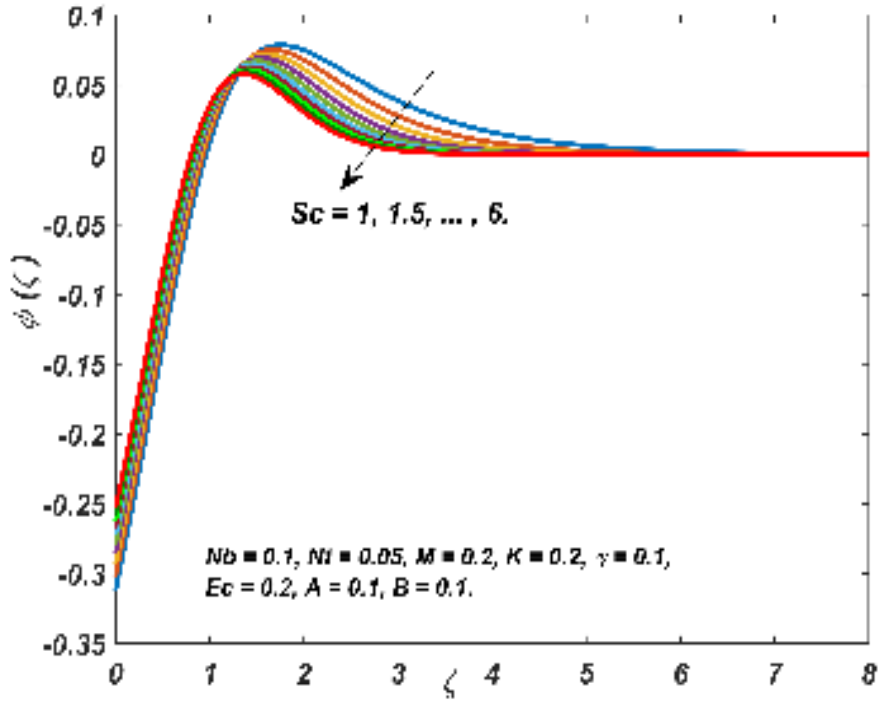

Figure 7.11: *Response in $\phi(\zeta)$ for distinct Sc.*

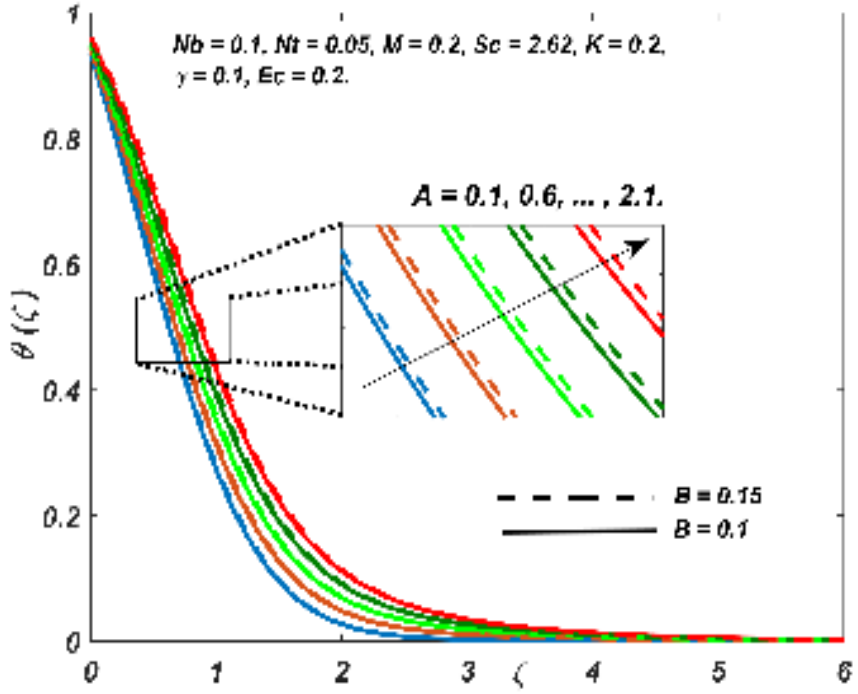

Figure 7.12: *Response in* $\theta(\zeta)$ *for distinct* $A \quad \& \quad B$.

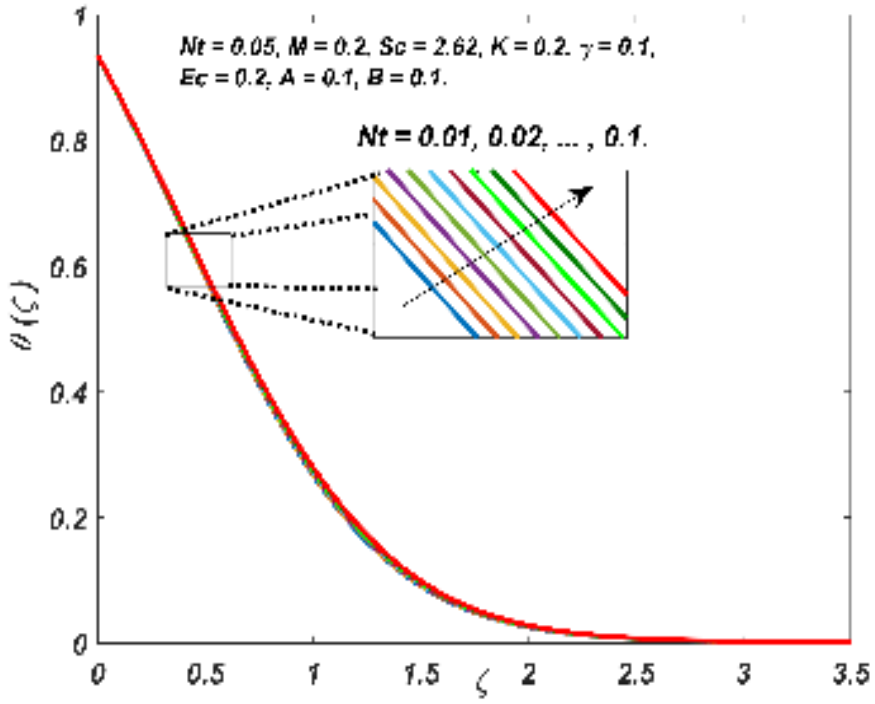

Figure 7.13: *Response in* $\theta(\zeta)$ *for distinct* Nt.

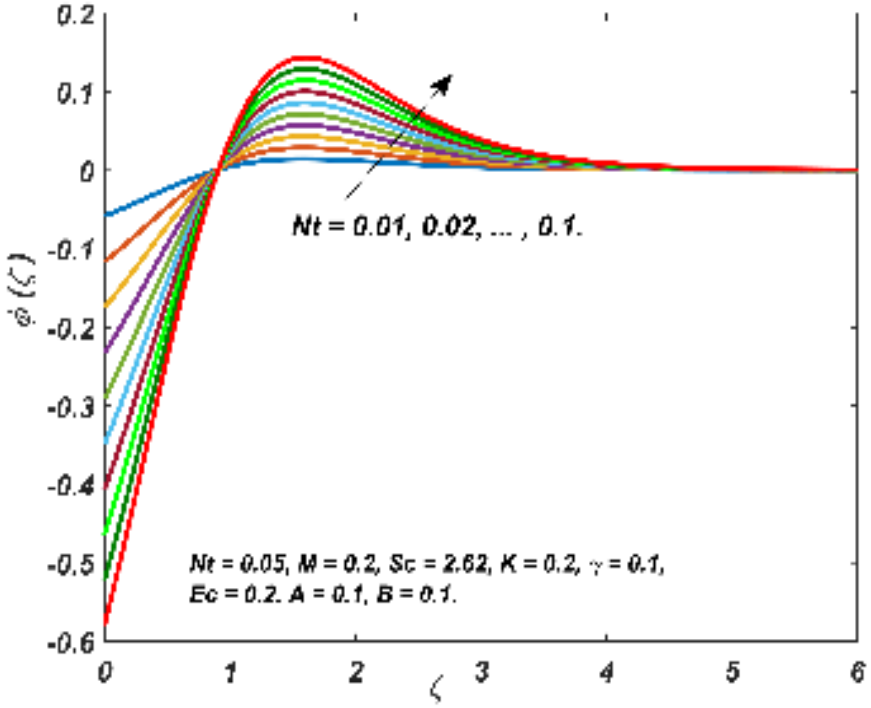

Figure 7.14: *Response in $\phi(\zeta)$ for distinct Nt.*

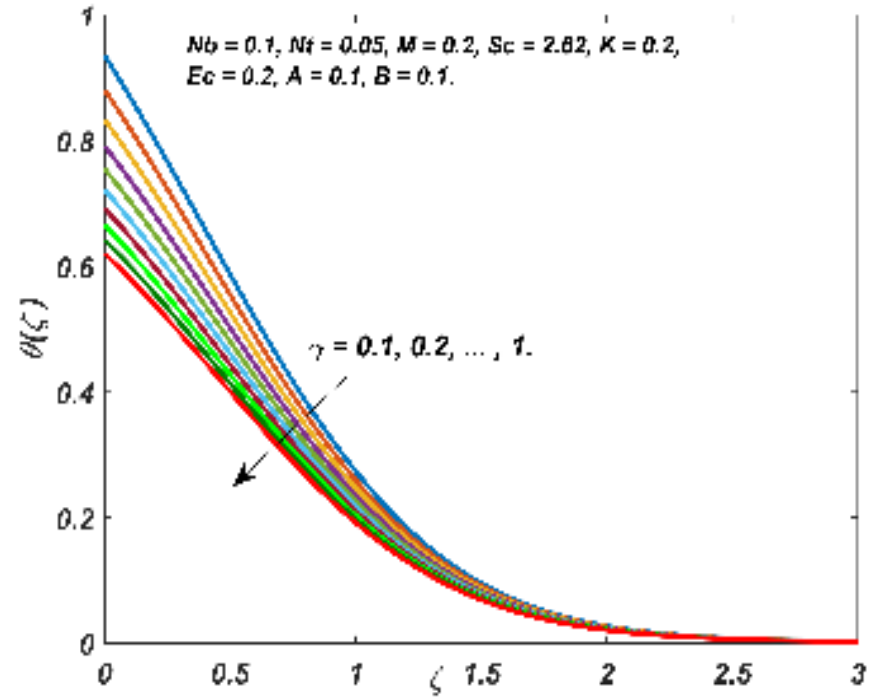

Figure 7.15: *Response in $\theta(\zeta)$ for distinct γ.*

Ec & Sc. Heat transfer rate is maximum for low Ec values. An increment in Ec escalates the temperature of the nanoliquid near the disk and hence it lowers the heat transfer rate. Heat transfer rate decreases with larger Nt (see Fig. 7.19). Physically, it is due to thermophoresis effects.

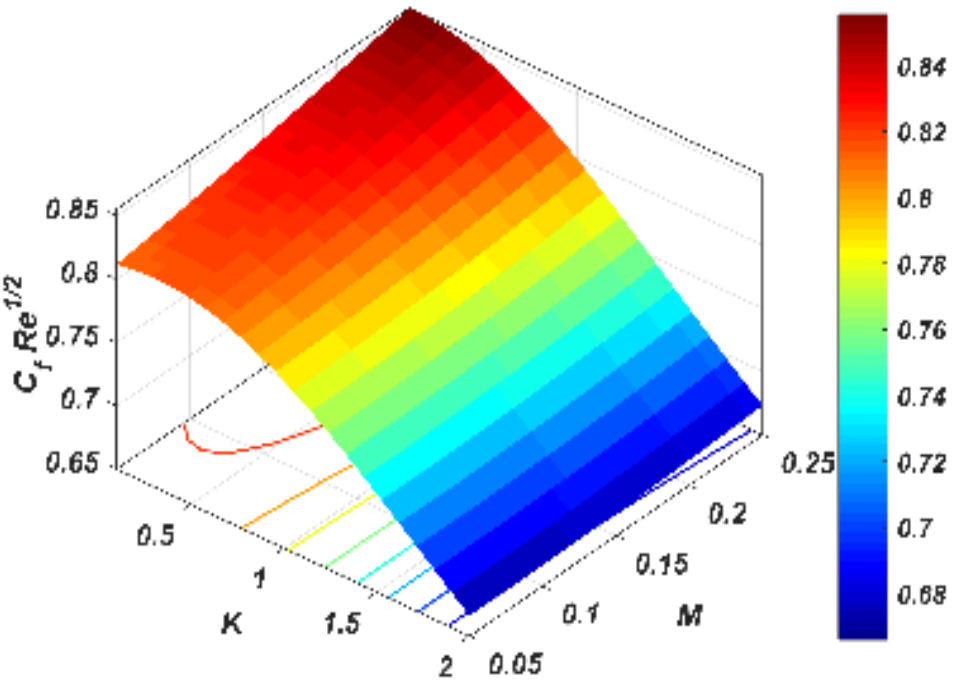

Figure 7.16: *Surface plot of* $C_f Re^{\frac{1}{2}}$ *for variation of* K *and* M.

7.5 Response Surface Methodology (RSM)

RSM is an experimental design-based statistical technique that illustrates the impact of influential parameters (independent variables) and their interactive effects on the physical quantity of choice (dependent or response variable). Experimental trials are time-consuming and costly whereas RSM reduces the number of trials and optimizes the response variable. RSM using the Central Composite Design (CCD) is a suitable sequential experimentation method which is incorporated in the present study with 20 ($2^j + 2j + o,\ j\ = 3, o = 6$) runs, here o denotes the number of faces and j denotes the number of factors. The relation involves 2^3 factorial 6 center and 6 axial points. A full quadratic 3 level factorial design is adopted in the study as follows

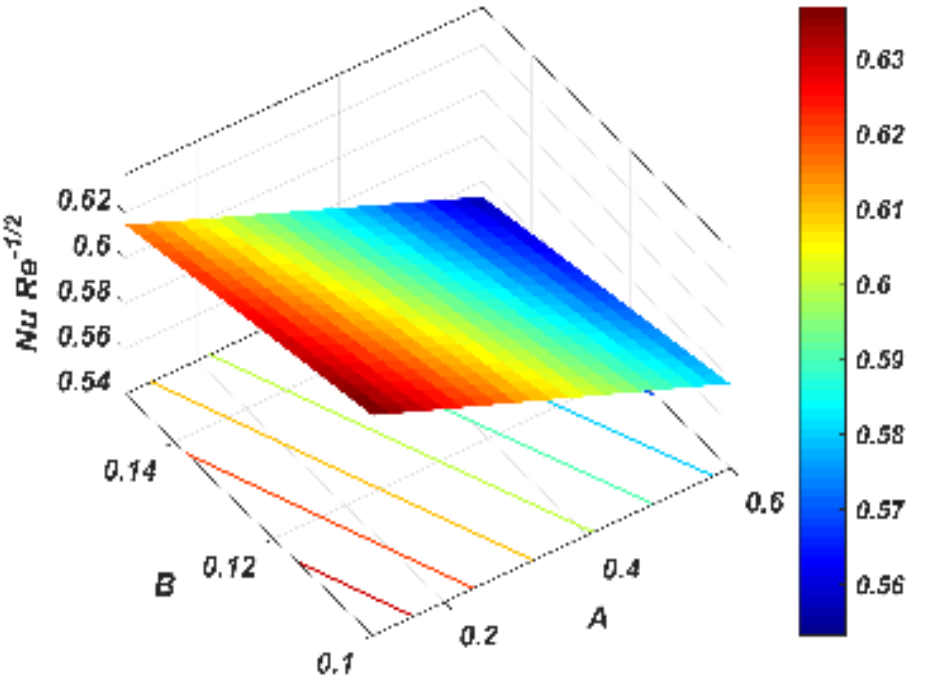

Figure 7.17: *Surface plot of* $NuRe^{-\frac{1}{2}}$ *for variation of* A *and* B.

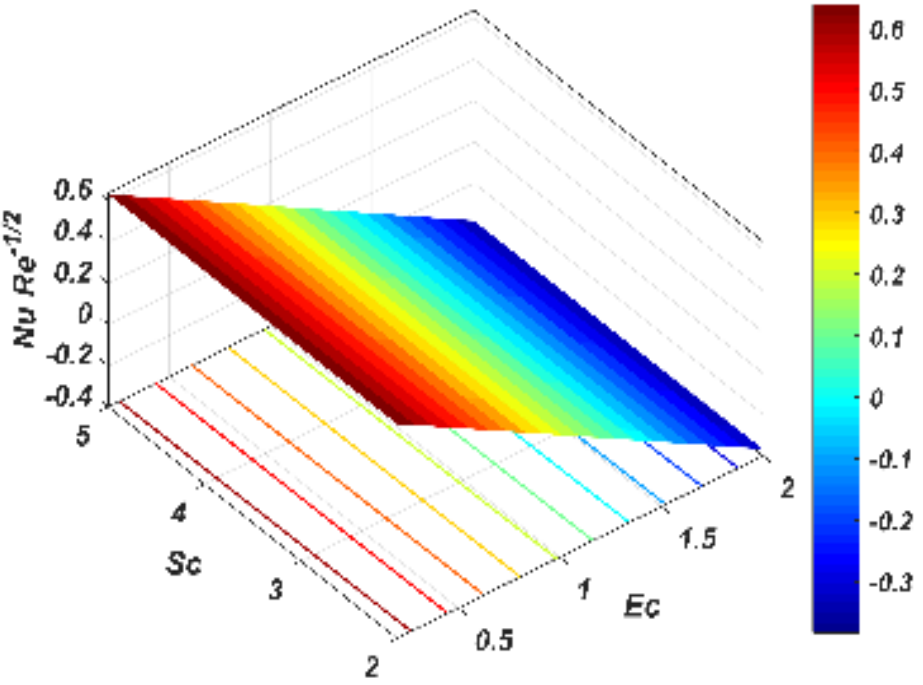

Figure 7.18: *Surface plot of* $NuRe^{-\frac{1}{2}}$ *for variation of* Sc *and* Ec.

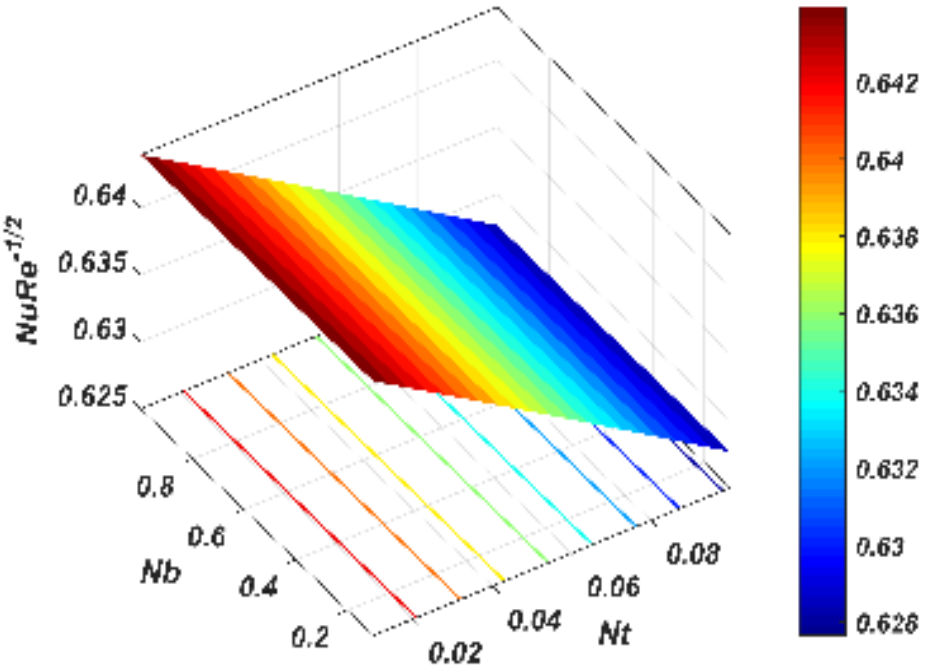

Figure 7.19: *Surface plot of* $NuRe^{-\frac{1}{2}}$ *for variation of* Nb *and* Nt.

$$\begin{aligned} Response\ (Y) = \ & L_1X_1 + L_2X_2 + L_3X_3 + L_4X_1X_2 + L_5X_2X_3 + L_6X_1X_3 + \\ & L_7X_1^2 + L_8X_2^2 + L_9X_3^2 + L_{10}. \end{aligned} \tag{7.5.1}$$

Here, L_i $(i = 1,\ 2,\ \ldots,\ 10)$ denote the regression coefficients. The RSM techniquie becomes advantageous in finding the levels of the parameters that optimize the response. In processes involving heat transfer, the maximization of the heat transfer is carried such that the desirability factor is maximized. If the lowest and highest response are respectively denoted by Y_l and Y_h, then the desirability factor is calculated as follows:

$$\begin{aligned} d &= 0, && Y \le Y_l \\ d &= \tfrac{Y - Y_l}{Y_h - Y_l}, && Y_l \le Y \le Y_h \\ d &= 1, && Y \ge Y_h \end{aligned} \tag{7.5.2}$$

For the present analysis, Nu_r is chosen as the response variable and the parameters inducted for the design are M $(0.15 \le M \le 2.5)$, K $(0.15 \le K \le 2.5)$, and γ $(0.05 \le \gamma \le 0.15\ )$ respectively. Also, the influential parameters M, K,

and γ are coded as X_1, X_2, and X_3 respectively (see Table 7.2). The numerical experimental design involving 20 runs (based on the face-centered CCD design) is given in Table 7.3.

The ANOVA table as described in Table 7.4 evaluates the quality of the fitted

Table 7.2: *The effectual levels of parameters.*

Parameters	Coded Symbols	Levels		
		-1 (Low)	0 (Medium)	1 (High)
M	X_1	0.15	0.2	0.25
K	X_1	0.15	0.2	0.25
γ	X_1	0.05	0.1	0.15

Table 7.3: *Experimental (numerical) design.*

Runs	Coded Values			Real values			Response
	X_1	X_2	X_3	M	K	γ	Nu_r
1	-1	-1	-1	0.15	0.15	0.05	0.716786
2	1	-1	-1	0.25	0.15	0.05	0.623955
3	-1	1	-1	0.15	0.25	0.05	0.700967
4	1	1	-1	0.25	0.25	0.05	0.604885
5	-1	-1	1	0.15	0.15	0.15	0.663199
6	1	-1	1	0.25	0.15	0.15	0.579336
7	-1	1	1	0.15	0.25	0.15	0.649497
8	1	1	1	0.25	0.25	0.15	0.562579
9	-1	0	0	0.15	0.2	0.1	0.681731
10	1	0	0	0.25	0.2	0.1	0.592045
11	0	-1	0	0.2	0.15	0.1	0.644742
12	0	1	0	0.2	0.25	0.1	0.628525
13	0	0	-1	0.2	0.2	0.05	0.661615
14	0	0	1	0.2	0.2	0.15	0.613698
15	0	0	0	0.2	0.2	0.1	0.636765
16	0	0	0	0.2	0.2	0.1	0.636765
17	0	0	0	0.2	0.2	0.1	0.636765
18	0	0	0	0.2	0.2	0.1	0.636765
19	0	0	0	0.2	0.2	0.1	0.636765
20	0	0	0	0.2	0.2	0.1	0.636765

quadratic model in a reliable way. The significance of linear, quadratic, and interactive regression terms of M,K, and γ are computed statistically using a high F value with p-value < 0.05. All the regression terms in the fitted model are significant (see Table 7.4). Fig. 7.20 is used to explain the accuracy of the fitted model. In

Table 7.4: *ANOVA table*

Source	Deg. of Freedom	Adj. Sum of Squares	Adj. Mean Squares	F-value	p-value
Model	9	0.026667	0.002963	827176.7	< 0.001
Linear terms	3	0.026615	0.008872	2476641	<0.001
M	1	0.020194	0.020194	5637544	< 0.001
K	1	0.000665	0.000665	185731.8	< 0.001
γ	1	0.005755	0.005755	1606648	< 0.001
Square terms	3	0.000004	0.000001	373.57	< 0.001
M^2	1	0	0	11.83	0.006
K^2	1	0	0	13.09	0.005
γ^2	1	0.000002	0.000002	611.68	< 0.001
Interaction terms	3	0.000049	0.000016	4515.58	< 0.001
$M \times K$	1	0.000005	0.000005	1387.84	< 0.001
$M \times \gamma$	1	0.000041	0.000041	11473.87	< 0.001
$K \times \gamma$	1	0.000002	0.000002	685.03	<0.001
Errors	10	0	0		
Lack-of-Fit	5	0	0	*	*
Pure Error	5	0	0		
Total	19	0.026667			
Coefficient of determination $\mathcal{R}^2 = 99.99$ %					

the normal probability plot against residuals, the data points are aligned along a straight line and the histogram has a bell shape. Therefore, the residuals follow a normal distribution. The maximum error entailed in the residual versus fitted value plots of the model is 0.00010. The coefficient of determination ($\mathcal{R}^2$) indicates the change in response variable for a chosen set of independent variables and the relevance of the model. The empirical model gives a good fit if $\mathcal{R}^2$ value is very close to 1. Here, $\mathcal{R}^2$ is found to be 99.99 % which guarantees the precision of the model.

7.5.1 Statistical Analysis

The fitted model of the response function Nu_r in terms of uncoded significant influential parameters is given below

$$\begin{aligned} Nu_r = {} & 0.910541 - 0.94622\,M - 0.10133\,K - 0.77684\,\gamma + 0.0497\,M^2 - 0.0522\,K^2 \\ & + 0.3570\,\gamma^2 - 0.31532\,M\,K + 0.90665\,M\,\gamma + 0.22153\,K\,\gamma \end{aligned} \tag{7.5.3}$$

The regression coefficients of M, K *and* γ are negative. These parameters have a negative impact with Nu_r. This indicates that heat transfer rate demotes an enhance in these parameters.

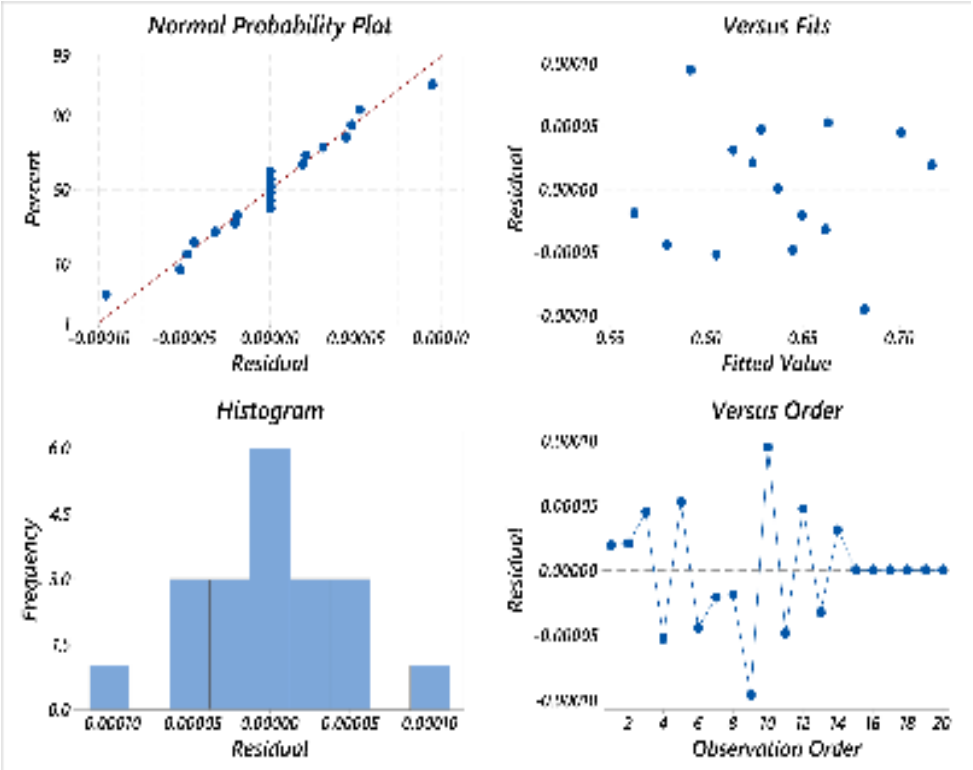

Figure 7.20: *Residual plots for* Nu_r.

Fig. 7.21-7.23 depict the simultaneous effect of pertinent parameters on Nu_r using contour and 3-D plots. The heat transfer coefficient is investigated by studying the interaction of two parameters while keeping the third parameter at a medium level. It can be noticed from Fig. 7.21 -7.23 that heat transfer coefficient is a decreasing function of M, K, and γ.

The optimization of heat transfer rate in practical applications implies the maximization of Nu_r, Therefore, the levels of the parameters that maximize the heat transfer rate are estimated to be $M = 0.15$ (low level), $K = 0.15$ (low level), and $\gamma = 0.05$ (low level). The maximized Nu_r value is estimated to be 0.7168 with a desirability of 0.9999.

7.5.2 Sensitivity analysis

The sensitivity of the heat transfer coefficient is estimated using the the full quadratic model with the coded coefficients given below:

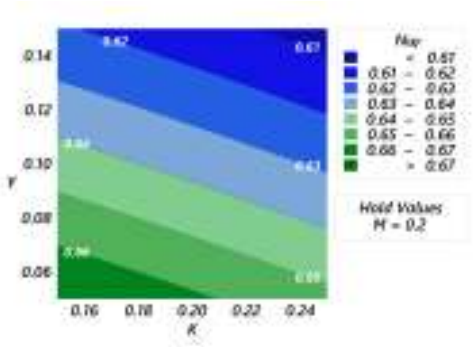

(a) *Contour plot of Nu_r for combinations of γ, K .*

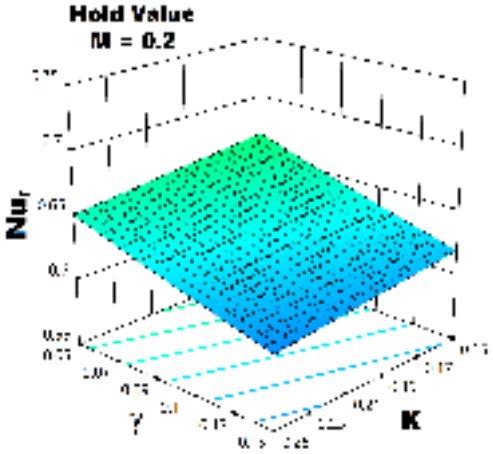

(b) *Response surface plot of Nu_r for combinations of γ, K .*

Figure 7.21: *Contour and response surface plot of Nu_r for combinations of γ, K .*

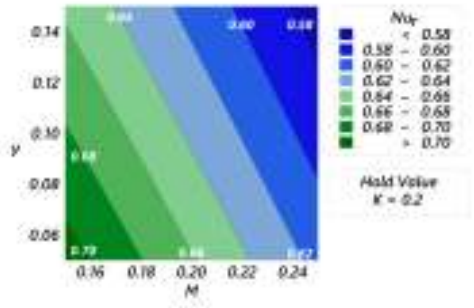

(a) *Contour plot of Nu_r for combinations of γ, M .*

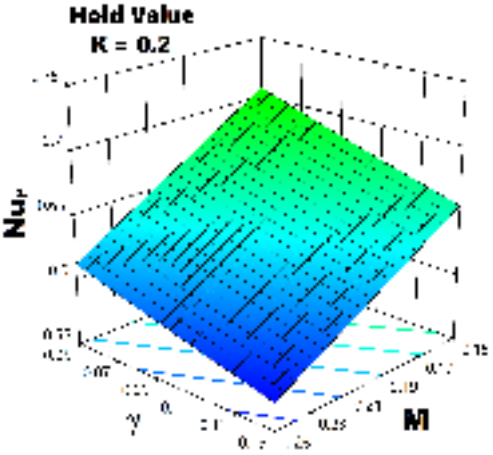

(b) *Response surface plot of Nu_r for combinations of γ, M .*

Figure 7.22: *Contour and response surface plot of Nu_r for combinations of γ, M .*

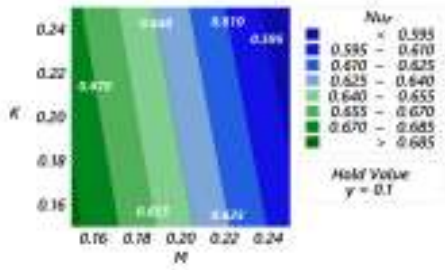

(a) *Contour plot of Nu_r for combinations of M, K .*

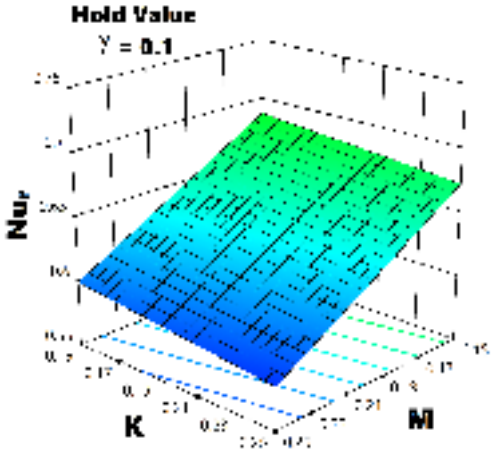

(b) *Response surface plot of Nu_r for combinations of M, K .*

Figure 7.23: *Contour and response surface plot of Nu_r for combinations of M, K .*

$$\begin{aligned} Nu_r = 0.636764 - 0.044938\ X_1 - 0.008157\ X_2 - 0.023990\ X_3 \\ +0.000124\ X_1^2 - 0.000131\ X_2^2 + 0.000893\ X_3^2 - 0.000788\ X_1X_2 \\ +0.002267\ X_1X_3 + 0.000554\ X_2X_3, \end{aligned} \tag{7.5.4}$$

The partial derivatives of the full quadratic model with the coded variables are computed to find the sensitivity functions as follows:

$$\frac{\partial Nu_r}{\partial X_1} = -0.044938 + 0.000248\ X_1 - 0.000788\ X_2 + 0.002267\ X_3, \tag{7.5.5}$$

$$\frac{\partial Nu_r}{\partial X_2} = -0.008157 - 0.000262\ X_2 - 0.000788\ X_1 + 0.000554\ X_3, \tag{7.5.6}$$

$$\frac{\partial Nu_r}{\partial X_3} = -0.023990 + 0.001786\ X_3 + 0.002267\ X_1 + 0.000554\ X_2. \tag{7.5.7}$$

Bar charts in Fig. 7.24 visualize the heat transfer coefficient sensitivity. Sensitivity is a measurement that interprets the level of change in response variables with variation in independent variables. The positive or negative sign in the sensitivity function indicates the nature of the sensitivity and its magnitude delineates the intensity of the relationship. The sensitivity of Nu_r is computed by assuming $M = 0.2$. Nu_r is negative sensitive towards M, K and γ. For a fixed value of K magnitude of sensitivity towards M, K and γ reduce with an increase in γ and the intensity of the relationship is maximum for M when compared to other variables. Further, the

sensitivity intensity augments with an increase in K. The change in the sensitivity rate with varying levels of γ is described as follows (see Table 7.5):

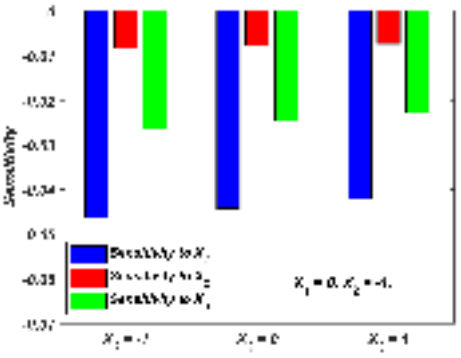

(a) *Bar charts depicting the sensitivity of Nu_r with $X_1 = 0, X_2 = -1$.*

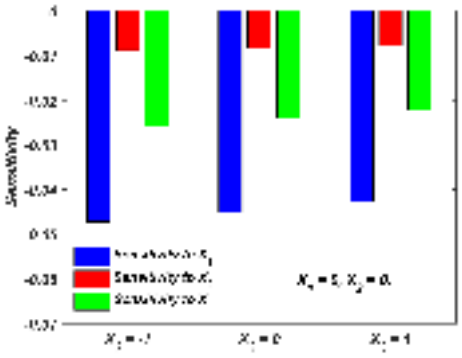

(b) *Bar charts depicting the sensitivity of Nu_r with $X_1 = 0, X_2 = 0$.*

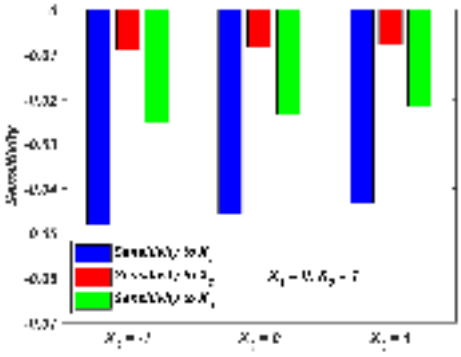

(c) *Bar charts depicting the sensitivity of Nu_r $X_1 = 0, X_2 = 1$.*

Figure 7.24: *Bar charts depicting the sensitivity of Nu_r*

- The sensitivity towards M varies at the rate of -0.2267%.
- The sensitivity towards K varies at the rate of -0.0554%.
- The sensitivity towards γ varies at the rate of -0.1786%.

Table 7.5: *The sensitivity values of the response Nu_r when $X_1 = 0$*

X_2	X_3	**Sensitivity values**		
		$\frac{\partial Nu_r}{\partial X_1}$	$\frac{\partial Nu_r}{\partial X_2}$	$\frac{\partial Nu_r}{\partial X_3}$
-1	-1	-0.046417	-0.008449	-0.02633
	0	-0.04415	-0.007895	-0.024544
	1	-0.041883	-0.007341	-0.022758
Rate of change		**-0.002267**	**-0.000554**	**-0.001786**
0	-1	-0.047205	-0.008711	-0.025776
	0	-0.044938	-0.008157	-0.02399
	1	-0.042671	-0.007603	-0.022204
Rate of change		**-0.002267**	**-0.000554**	**-0.001786**
1	-1	-0.047993	-0.008973	-0.025222
	0	-0.045726	-0.008419	-0.023436
	1	-0.043459	-0.007865	-0.021650
Rate of change		**-0.002267**	**-0.000554**	**-0.001786**

7.6 Conclusions

An electrically conducting Reiner Rivlin nanoliquid flow past a rotating disk is considered in the study. A uniform magnetic field of intensity B_0 is applied along the axial direction. The volume fraction of the nanoparticles on the surface of the disk is passively controlled by a realistic boundary condition . In addition, thermal jump conditions and Joule heating effects are accounted. In the presence of a space-dependent and temperature- dependent heat source effects the conclusions of the present work are summarized below:

- Radial and azimuthal velocities demote with an increment in magnetic field due to the presence of Lorentz force.
- Radial velocity and surface drag decrease with augmentation in Reiner-Rivlin fluid parameter. It is due to an elevation in the cross-viscosity coefficient.
- The temperature profile increases due to both temperature and space-dependent heat sources. An opposite trend is noted in the heat transfer rate.
- Joule heating has a positive influence on the thermal boundary layer. The heat transfer rate lowers with an increment in the Eckert number.
- Hartmann number, Reiner-Rivlin fluid parameter, and thermal slip parameter show a negative response with heat transfer coefficient.

- The heat transfer sensitivity towards the Hartmann number decreases at the rate of 0.2267% and the sensitivity towards the Reiner-Rivlin fluid parameter decreases at the rate of 0.0554% when thermal slip is incremented.